

## Regional Climatic Effects According to Different Estimations of Biogenic Volatile Organic Compounds during the Asian Summer Monsoon

Hyung-Jin Kim<sup>1</sup>, Kumiko Takata<sup>2\*</sup>, Katsunori Tanaka<sup>2</sup>, Ryoji Yamashima<sup>3</sup>, Jun Matsumoto<sup>2,3</sup>, Kazuyuki Saito<sup>2</sup>, Toshihiko Takemura<sup>4</sup>, and Tetsuzo Yasunari<sup>5</sup>

<sup>1</sup>Climate Research Department, APEC Climate Center, Busan, Korea

<sup>2</sup>Research Institute for Global Change, Japan Agency for Marine-Earth Science and Technology, Yokohama, Japan

<sup>3</sup>Department of Geography, Tokyo Metropolitan University, Tokyo, Japan

<sup>4</sup>Research Institute for Applied Mechanics, Kyushu University, Fukuoka, Japan

<sup>5</sup>Research Institute for Humanity and Nature, Kyoto, Japan

(Manuscript received 29 August 2013; accepted 1 February 2014)

© The Korean Meteorological Society and Springer 2014

**Abstract:** A series of 60-year numerical experiments starting from 1851 was conducted using a global climate model coupled with an aerosol-cloud-radiation model to investigate the response of the Asian summer monsoon to variations in the secondary organic aerosol (SOA) flux induced by two different estimations of biogenic volatile organic compound (BVOC) emissions. One estimation was obtained from a pre-existing archive and the other was generated by a next-generation model (the Model of Emissions of Gases and Aerosols from Nature, MEGAN). The use of MEGAN resulted in an overall increase of the SOA production through a higher rate of gas-to-particle conversion of BVOCs. Consequently, the atmospheric loading of organic carbon (OC) increased due to the contribution of SOA to OC aerosol. The increase of atmospheric OC aerosols was prominent in particular in the Indian subcontinent and Indochina Peninsula (IP) during the pre- and early-monsoon periods because the terrestrial biosphere is the major source of BVOC emissions and the atmospheric aerosol concentration diminishes rapidly with the arrival of monsoon rainfall. As the number of atmospheric OC particles increased, the number concentrations of cloud droplets increased, but their size decreased. These changes represent a combination of aerosol-cloud interactions that were favorable to rainfall suppression. However, the modeled precipitation was slightly enhanced in May over the oceans that surround the Indian subcontinent and IP. Further analysis revealed that a compensating updraft in the surrounding oceans was induced by the thermally-driven downdraft in the IP, which was a result of surface cooling associated with direct OC aerosol radiative forcing, and was able to surpass the aerosol-cloud interactions. The co-existence of oceanic ascending motion with the maximum convective available potential energy was also found to be crucial for rainfall formation. Although the model produced statistically significant rainfall changes with locally organized patterns, the suggested pathways should be considered guardedly because in the simulation results, 1) the BVOC-induced aerosol direct effect was marginal; 2) cloud-aerosol interactions were model-dependent; and 3) Asian summer monsoons were biased to a non-negligible extent.

**Key words:** Biogenic volatile organic compounds, East Asia summer monsoon, coupled global climate model, aerosol direct effect, aerosol-cloud interactions

### 1. Introduction

Atmospheric aerosols, which largely consist of a mixture of sulfates, carbonaceous particles [black carbon (BC) and organic carbon (OC)], soil dust, and sea salt, play a crucial role in the global climate system. Aerosols directly modulate the terrestrial radiation budget by scattering or absorbing radiation. Additionally, aerosol activation, a process in which suspended particles grow to form cloud droplets, indirectly affects the microphysical and optical properties of clouds. Aerosol particles with the potential to nucleate liquid cloud droplets are termed 'cloud condensation nuclei' (CCN), while those particles that induce ice crystal formation are termed 'ice nuclei' (IN).

Atmospheric aerosols play various roles in the global energy balance. For example, BC particles absorb solar radiation because of their high absorptivity in the visible wavelengths, thus leading to a tropospheric warming (Jacobson, 2001). In contrast, non-absorbing aerosols, such as sulfate, increase the reflection of sunlight back to space (Charlson *et al.*, 1991), thereby opposing the effects of infrared-active gases (Tett *et al.*, 1999). The absorption of solar radiation by BC particles results in surface warming at a distance through dynamical heat transport, but locally it lowers surface temperature by reducing the insolation reaching the ground (Menon *et al.*, 2002). Aerosol-cloud interactions also rely on the properties of aerosol constituents such as number concentration, particle size, and chemical traits. When clouds form with elevated concentrations of the accumulation size modes (particles in the size range of 0.001-0.1  $\mu\text{m}$  radius), precipitation is suppressed because the higher concentration of smaller cloud droplets delays coalescence (Albrecht, 1989; Rosenfeld *et al.*, 2007). Conversely, the presence of large CCN (radius greater than 5  $\mu\text{m}$ ) facilitates precipitation processes, which adds uncertainty to the indirect effects of atmospheric aerosols (Johnson, 1982; Rosenfeld *et al.*, 2002).

\*Current affiliation: Arctic Environment Research Center, National Institute of Polar Research, Tokyo, Japan

Corresponding Author: Hyung-Jin Kim, APEC Climate Center, 12 Centum 7-ro, Haeundae-gu, Busan 612-020, Korea.

E-mail: hyungjin@apcc21.org

In recent decades, researchers have used global climate models (GCMs) to investigate climate responses to these aerosol effects in tandem with new remote-sensing technology and analysis methodology. Early GCM studies mainly used sulfate particles to represent anthropogenic aerosols (Jones *et al.*, 1994; Boucher and Lohmann, 1995), whereas more recent GCMs have also considered carbonaceous aerosols. The modeling results have suggested considerable modification of energy and water cycles (Menon *et al.*, 2002; Ramanathan *et al.*, 2005; Lau *et al.*, 2006; Bollasina *et al.*, 2011). However, determining the global distribution of aerosol properties, especially the formation and global budget of organic aerosols (OAs), is a major challenge (Hallquist *et al.*, 2009). OAs are categorized as either primary (POAs) or secondary (SOAs). Previous studies have shown that SOA can become the main fraction of OC particles under certain circumstances (Kanakidou *et al.*, 2005, and references therein). SOA is produced by the atmospheric photo-oxidation of volatile organic compounds (VOCs), which are predominantly emitted from the Earth's biosphere (Kuhn *et al.*, 2004). In recognition of such relationships, researchers have tried to assess the effects of biogenic VOC (BVOC) on climate variations using numerical models (Collins *et al.*, 2002; Sanderson *et al.*, 2003; Tsigaridis and Kanakidou, 2007). The emission inventories adopted in previous numerical studies were produced by early versions of BVOC emission models developed in the 1990s (Pierce and Waldruff, 1991; Graedel *et al.*, 1993; Guenther *et al.*, 1995; Pierce *et al.*, 1998). However, these versions are expected to be replaced with a next-generation model: the Model of Emissions of Gases and Aerosols from Nature (MEGAN), which was recently devised by Guenther *et al.* (2006). Therefore, addressing the differences in BVOC estimations and the resulting differences in the simulated climatic roles of BVOC will be informative to modeling communities.

In this study, BVOC emissions obtained from both pre-existing inventories and modern algorithms were used to drive a global aerosol transport-radiation model implemented with a coupled GCM (CGCM). Two 60-year numerical integrations using 1851 as a starting point were then undertaken to test the sensitivity of the model simulations to the different BVOC emissions. These integrations were designed to examine the effects of changes in BVOC emissions induced by anthropogenic land cover/land use changes. During the 18th and 19th centuries, India and China experienced a large expansion in cultivation, which converted forest to cropland (Ramankutty and Foley, 1999; Hirabayashi *et al.*, 2005). The simulations used in this study represent the climate in the 19th century, and additional simulations with conditions in the 1700s are in progress to reproduce the 18th century climate. By comparing these simulations, the effects of changes in biogenic aerosol emissions associated with land management practices can be explored. However, in this study, we used the 1851 integrations to investigate the climatic role of variations in BVOC emissions with a particular focus on the effects of BVOC-induced aerosols on the regional hydrological cycle during the Asian

summer monsoon.

The remainder of this report is organized as follows. The modeling systems, a brief description of BVOC estimations, and numerical experiments are presented in section 2. Section 3 analyzes changes in atmospheric aerosols and the associated aerosol radiative forcings in the model outcomes. In section 4, the fidelity of the climatological monsoon precipitation is validated and the simulated aerosol-cloud interactions are investigated. Section 5 describes the possible mechanisms through which the BVOC-induced atmospheric aerosols affect regional precipitation. The results are summarized and discussed in the final section.

## 2. Model description, BVOC estimations, and numerical simulations

### a. Model description

The CGCM used in this study was the latest version of the Model for Interdisciplinary Research on Climate (MIROC5) developed jointly at the Center for Climate System Research at the University of Tokyo, National Institute for Environmental Studies, and the Japan Agency for Marine-Earth Science and Technology. MIROC5 is composed of a full ocean model with an approximately  $1^\circ$  mesh in the horizontal and 49 levels in the vertical, and an atmospheric model with T42 resolution ( $128 \times 64$  grids) in the horizontal and 40 sigma levels in the vertical. Readers are referred to Watanabe *et al.* (2010) for a comprehensive description of the physical parameterizations and dynamical core of MIROC5.

The aerosol effects were calculated using the Spectral Radiation-Transport Model for Aerosol Species (SPRINTARS) (Takemura *et al.*, 2000, 2002, 2005, 2009), which when incorporated into MIROC5 allows interactions among the atmospheric dynamics, aerosol cycle, and hydrological cycle. SPRINTARS predicts mass mixing ratios for the major tropospheric aerosols (BC, OC, sulfate, soil dust, and sea salt) and the sulfate precursor gases [sulfur dioxide ( $\text{SO}_2$ ) and dimethyl sulfide (DMS)] for atmospheric sulfate particles. Aerosol transport processes include emission, advection, diffusion, sulfur chemistry, wet deposition, dry deposition, and gravitational settling.

The radiation scheme in MIROC5 adopting the two-stream discrete ordinate and adding method (Nakajima *et al.*, 2000) includes a calculation of the aerosol direct effect. Scattering and absorption coefficients depending on the wavelength, prescribed size distributions, and hygroscopic growth are considered for each type of aerosol. The refractive indices used for dry aerosols are taken from Deepak and Gerber (1983). The model treats not only the cloud mass mixing ratios, but also the cloud droplet and icy crystal number concentrations, as prognostic variables. The nucleation of the cloud droplets follows Abdul-Razzak and Ghan (2000), who developed a parameterization based on Köhler theory (Takemura *et al.*, 2005). The formation of ice crystals includes both homoge-

neous and heterogeneous processes (Takemura *et al.*, 2009). Changes in the cloud droplet and ice crystal number concentrations induce changes in the cloud droplet and ice crystal effective radii, respectively. The precipitation rate for warm rain depends on the cloud droplet number concentration and the cloud water mixing ratio according to Berry (1967). However, a change in the precipitation rate for cold rain is not included in the present version of SPRINTARS. A detailed description of SPRINTARS is given in Takemura *et al.* (2002) for the direct effect and in Takemura *et al.* (2005, 2009) for the indirect effect.

The fidelity of the modeling systems in reproducing aerosol optical depth and cloud fields (such as cloud droplet effective radius and cloud radiative forcing) has been validated against ground-based measurements and satellite remote sensing retrievals (Takemura *et al.*, 2002, 2005). SPRINTARS was also used in an intercomparison project for global aerosol models, where uncertainties in simulated parameters were estimated (Textor *et al.*, 2007; Quaas *et al.*, 2009).

### b. BVOC estimations

Unlike the early versions of BVOC algorithms that utilize the canopy dry mass, ecosystem-dependent factors, leaf temperature, and photosynthetically active radiation (e.g., Guenther *et al.*, 1995), MEGAN also considers cumulative leaf area index ( $\lambda_{\text{LAI}}$ ), soil moisture ( $\lambda_{\text{SM}}$ ), the production or loss of BVOC within the canopy ( $\rho$ ), and more complex light and temperature functions. Briefly, the  $\lambda_{\text{LAI}}$  considers the impact of leaf age (i.e., new, growing, mature, and old foliage) on isoprene and monoterpene emissions (Guenther *et al.*, 1991). The LAI of the previous and current month as well as monthly surface air temperature can be used to estimate the LAI of each age group. Moreover, monoterpenes, whose SOAs are of primary importance for global organic aerosols (Chung and Seinfeld, 2002; Engelhart *et al.*, 2008), are subdivided into eight components, while previous versions usually treat them as a whole. Accordingly, the emission and light-dependence factors for monoterpenes in MEGAN differ from one component to another. Here, the values for  $\rho$  and  $\lambda_{\text{SM}}$  were assumed to be unity.

Lathière *et al.* (2010) estimated isoprene emissions calculated by MEGAN. They reported that the model reproduces the above-canopy flux measurements and the site-to-site variability reasonably well. They also recognized some underestimation in isoprene emissions but argued that such disagreement could be corrected when the regional variability of emission factors for particular plant functional types is considered. However, monoterpene emissions from MEGAN have seldom been validated due to a scarcity of observations. In general, the lack of time-resolved and accurate inventories has introduced large uncertainties in estimated BVOC emissions. Consequently, the published global BVOC budgets differ significantly (Kanakidou *et al.*, 2005). The results presented in this study, therefore, should be viewed as the response of a CGCM to differing

BVOC estimations, where observational uncertainties exist.

### c. Numerical experiments

A transient simulation was first performed for 150 years from 1851 following the standards of ‘historical run’ in the Coupled Model Intercomparison Project Phase 5 (Taylor *et al.*, 2012). Next, a control run (CTL) and a counterpart run (EXP) were performed for 60 years using the final restart files of the transient simulation and the historical boundary data sets of the 19th century (further details of the historical data are described below). However, it should be noted that only the results from the last 40 years were presented from both the CTL and EXP experiments, because the first 20 years were regarded as a spin-up period. We confirmed that no significant trends appeared in the atmosphere and the near surface land and ocean in the simulations for the final 40-year period.

The CTL and EXP experiments used retrospective estimations from vegetation maps and the corresponding LAI distribution reconstructed by Ramankutty and Foley (1999) and Hirabayashi *et al.* (2005). The atmospheric concentrations of well-mixed greenhouse gases ( $\text{CO}_2$ ,  $\text{CH}_4$ , and  $\text{N}_2\text{O}$ ) and the tropospheric oxide forms of OH and  $\text{H}_2\text{O}_2$  for sulfate chemistry were based on the Representative Concentration Pathways Concentration Calculations and Data (RCP-CCD), which is available online at <http://www.pik-potsdam.de/~mmalte/rcps/index.htm> (Meinshausen *et al.*, 2011). The concentrations of  $\text{CO}_2$ ,  $\text{CH}_4$ , and  $\text{N}_2\text{O}$  were set to 284.725 ppm, 790.979 ppb, and 275.425 ppb, respectively. The three-dimensional atmospheric concentrations of ozone were pre-calculated using a chemical model (Sudo *et al.*, 2002), driven with emissions of ozone precursors under conditions in 1850 given by the RCP-CCD. The historical data used to determine total solar irradiance and volcanic aerosols were taken from Lean *et al.* (2005) and Sato *et al.* (1993), respectively.

SOA is produced by atmospheric chemical reactions of VOC. However, the modeling system used in this study does not include those reactions on-line, hence the SOA production (or SOA production rate) was precalculated based on the BVOC using a chemical model (Sudo *et al.*, 2002), and prescribed as a boundary condition. For convenience, therefore, the SOA production at the surface for a unit time and area was treated similarly to a flux in units of  $\text{kg m}^{-2} \text{sec}^{-1}$ .

The CTL was performed with a climatological monthly mean SOA produced from BVOC emission taken from the United Nations and Global Emissions Inventory Activities (GEIA) database, while the EXP was performed with SOA from the BVOC flux calculated from MEGAN. The meteorological variables required for MEGAN, such as surface air temperature and downward shortwave radiation, were provided from the monthly climatology of the CTL simulation. Given the same meteorological conditions, differences in surface BVOC emissions will arise from the biogenic and radiative sensitivity in the two BVOC algorithms, which then act as perturbations in the EXP simulation.

**Table 1.** A brief description of the aerosol emission flux for numerical experiments (BC: black carbon, OC: organic carbon, SOC: secondary OC, SOA: secondary organic aerosol, VOC: volatile organic compound, DMS: dimethyl sulfide).

Subspecies		Emission flux
1. BC		Prescribed
2. Total OC (OC + SOC)	OC SOC	Prescribed From SOA that is produced from VOC (VOC emissions are different among the numerical experiments due to different estimations)
3. Sea salt		SPRINTARS (10-m wind speed)
4. Soil dust		SPRINTARS (vegetation, 10-m wind speed, leaf area index, soil moisture, snow)
5. Sulfate (SO <sub>2</sub> + DMS)	SO <sub>2</sub> DMS	Prescribed SPRINTARS (from oceanic phytoplankton and land sources as a function of the surface downward solar flux)

Our modeling systems included atmospheric aerosols of BC, total OC (the sum of OC and secondary OC), sea salt, soil dust, and sulfate (the sum of SO<sub>2</sub> and DMS) (Table 1). Surface emissions of BC, OC, and SO<sub>2</sub> from various sources were prescribed using the RCP-CCD. In contrast, soil dust levels were calculated using MIROC5's internal parameters: vegetation, 10-m wind speed, LAI, soil moisture, and amount of snow cover (Takemura *et al.*, 2009). Likewise, emissions of DMS (largely from oceanic phytoplankton but also including minor sources from land) and sea salt particles were determined from a simple function of the surface downward shortwave flux and 10-m wind speed, respectively (Takemura *et al.*, 2000, 2009). Differences also appeared in the production of secondary OC (SOC) aerosols originating from the gas-to-particle conversion of BVOC. This was because the BVOC emissions were determined by GEIA in the CTL simulation, whereas in the EXP, the surface BVOC flux was estimated by MEGAN. Table 1 summarizes the aerosol species and their emission fluxes used in the numerical experiments.

### 3. Atmospheric aerosols and aerosol radiative forcings

Figure 1 presents the climatological annual-mean SOA production from the CTL simulation and the differences between the EXP and CTL simulations. The main source of SOA was the biosphere in the tropics and subtropics, with local maximums appearing at the eastern coast of India, the IP, and the maritime continent (MC). The BVOC estimation from MEGAN resulted in an overall increase in SOA production over most vegetated areas. The changes were regionally as large as the SOA production in the CTL in tropical rain forest, with the largest increase at the IP.

Figure 2a displays the climatological summer-mean total aerosol optical depth (TAOD) at the wavelength of 550 nm obtained from the CTL simulation (shading), and the differences between the two experiments (contours). TAOD values were high over the Arabian Peninsula and eastern Middle East, but decreased gradually to the southeast. The differences in TAOD revealed a bipolar structure over the Middle East with a positive polarity over Pakistan. A secondary change in TAOD occurred across a broader area over the IP, MC and Southeast Asia where the background TAOD value was relatively low.

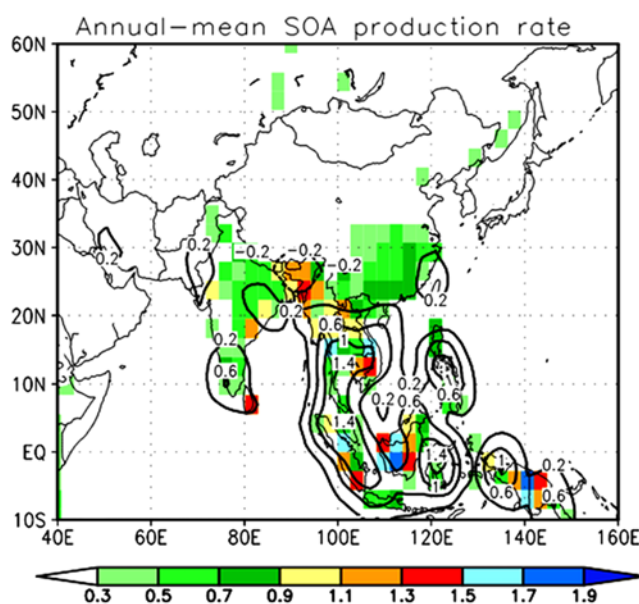


**Fig. 1.** Annual-mean secondary organic aerosol (SOA) from the CTL simulation (shading) and the differences between the EXP and CTL simulations (contour). Units are  $10^{-11} \text{ kg m}^{-2} \text{ s}^{-1}$ .

To identify the dominant aerosol components for the changes in TAOD, the differences in AOD were calculated for each aerosol species (BC, total OC, sea salt, dust, and sulfate as listed in Table 1) and plotted in Fig. 2b with contour intervals that are the same as in Fig. 2a. The results indicate that given the identical scale, only the changes in dust and total OC aerosols are visible and the changes in TAOD are almost completely explained by the changes in these two species.

Figure 2c shows the time-latitude TAOD distribution derived from the CTL simulation and the differences between the two experiments, while Fig. 2d shows the time-latitude AOD differences for each aerosol component. The Indian summer monsoon at the longitude from 70°E to 90°E was selected to calculate the area average. Note that the contour intervals are the same as in Figs. 2c, d, and again only dust and total OC changes are shown in Fig. 2d. Two prominent regions appear in the CTL's climatological TAOD (shading in Fig. 2c), one at the northern flank of the Tibetan Plateau (TP) at around 40°N, which began to build up from spring and matured in August,

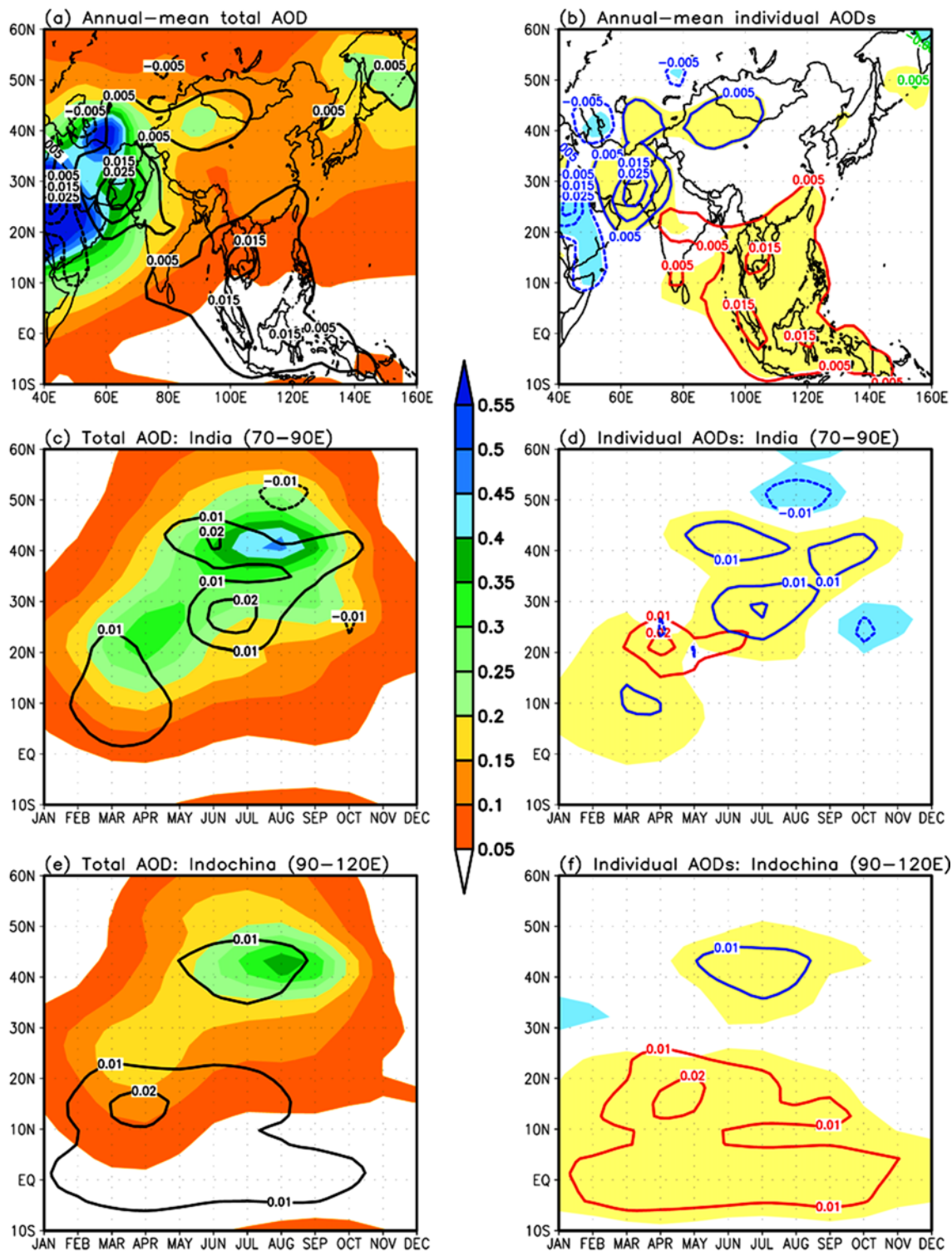


**Fig. 2.** (left) Total aerosol optical depth (TAOD) at 550 nm for the CTL simulation (shading) and (right) the differences between the EXP and CTL simulations (contour). Differences in individual AODs at 550 nm with TAOD differences greater than  $\pm 0.005$  (positive in yellow and negative in blue). (a)-(b) Annual mean; (c)-(d) Time-latitude distributions averaged over the Indian subcontinent (70-90°E); and (e)-(f) Time-latitude distributions averaged over the Indochina Peninsula (90-120°E). Individual AOD differences were calculated separately for the five aerosol species [BC, total OC (the sum of OC and SOC), sea salt, soil dust, and sulfate] and then plotted in the right panels with the same contour intervals used in the left panels. The results indicate that only total OC (red contours) and dust particle aerosol (blue contours) show measurable changes.

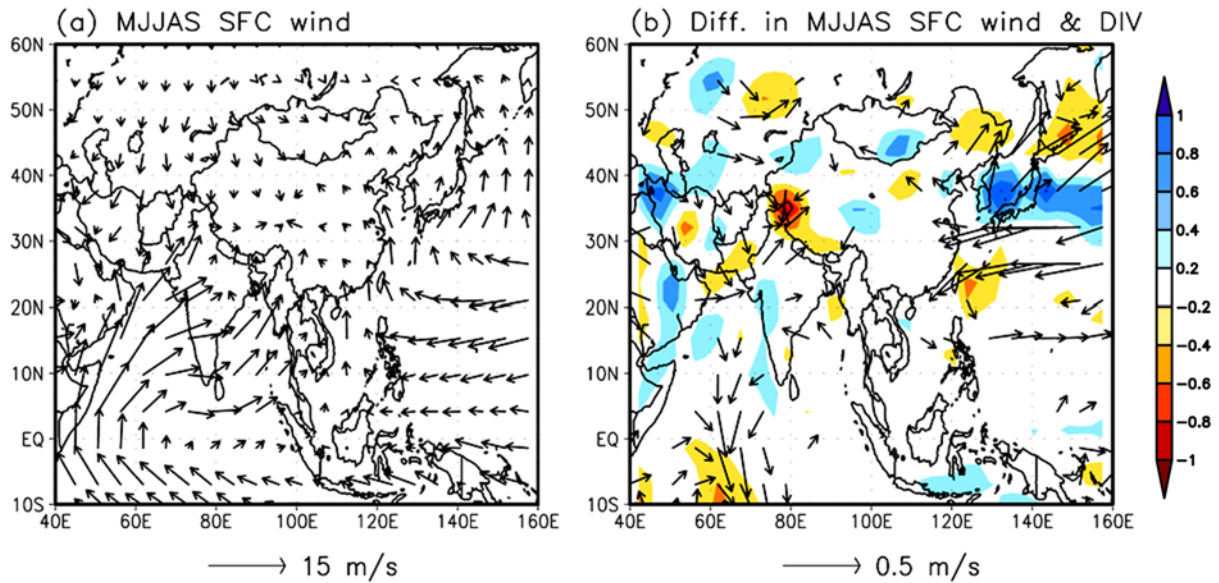


**Fig. 3.** (a) MJJAS climatology of 10-m wind ( $\text{m s}^{-1}$ ) from the CTL simulation and (b) the differences (vector,  $\text{m s}^{-1}$ ) between the EXP and CTL experiments. Also shown in (b) are the differences in the horizontal divergence of climatological MJJAS 10-m winds (shadings,  $10^{-6} \text{ s}^{-1}$ ).

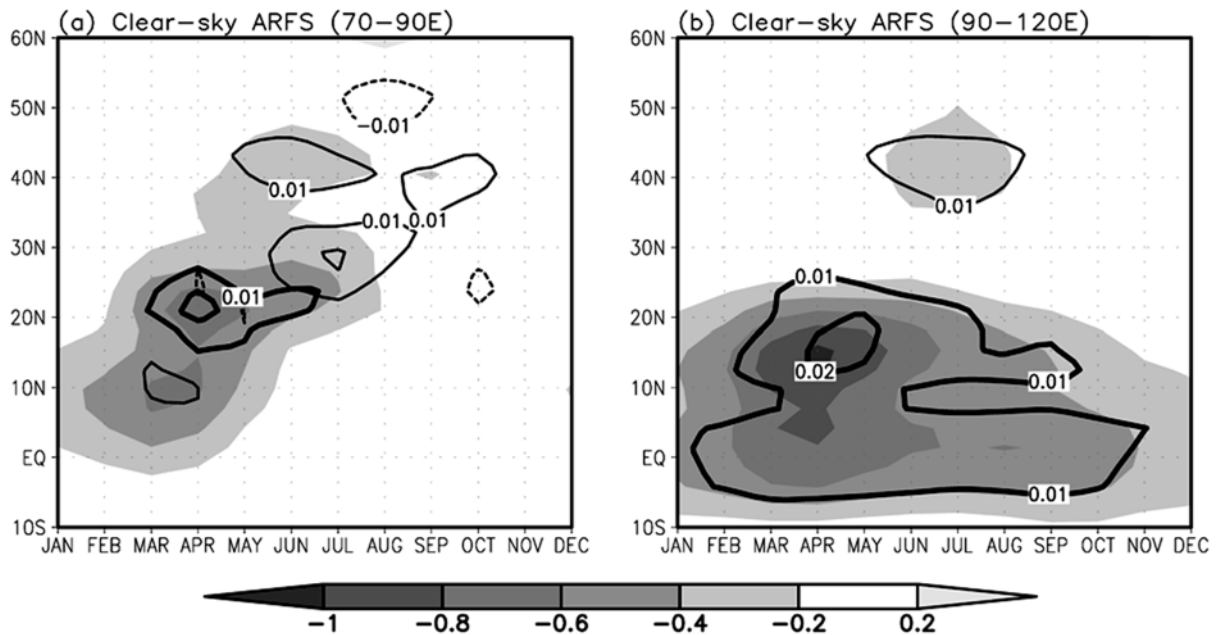


**Fig. 4.** Time-latitude distributions of the differences in aerosol radiative forcing at the surface (ARFS,  $\text{W m}^{-2}$ ) between the EXP and CTL simulations (shading) averaged over (a) the Indian subcontinent (70–90°E) and (b) the Indochina Peninsula (90–120°E). The ARFS (positive downward) is defined as the summation of both longwave and shortwave aerosol radiative forcings under clear-sky conditions. Also shown are the differences in AOD for total OC (thick contours) and dust aerosol (thin contours).

and the other over India at 15–30°N, which peaked in April and May. TAOD values in the EXP simulation were higher than in the CTL simulation (black contour in Fig. 2c), which is attributed to higher levels of dust aerosol (blue contour in Fig. 2d) and total OC particles (red contour in Fig. 2d). The source of the increased dust aerosol at around 30°N and 40°N seems to be a slightly enhanced local convergence of desert dust in

Pakistan and the Taklimakan Desert, respectively (Fig. 3), although the causes of such circulation changes are inexplicable. The excessive total OC aerosol in India between 15°N and 30°N is obviously a result of the increased SOA production (see Fig. 1).

The monthly variations in TAOD and the dominant role of dust and total OC aerosols in determining temporal TAOD

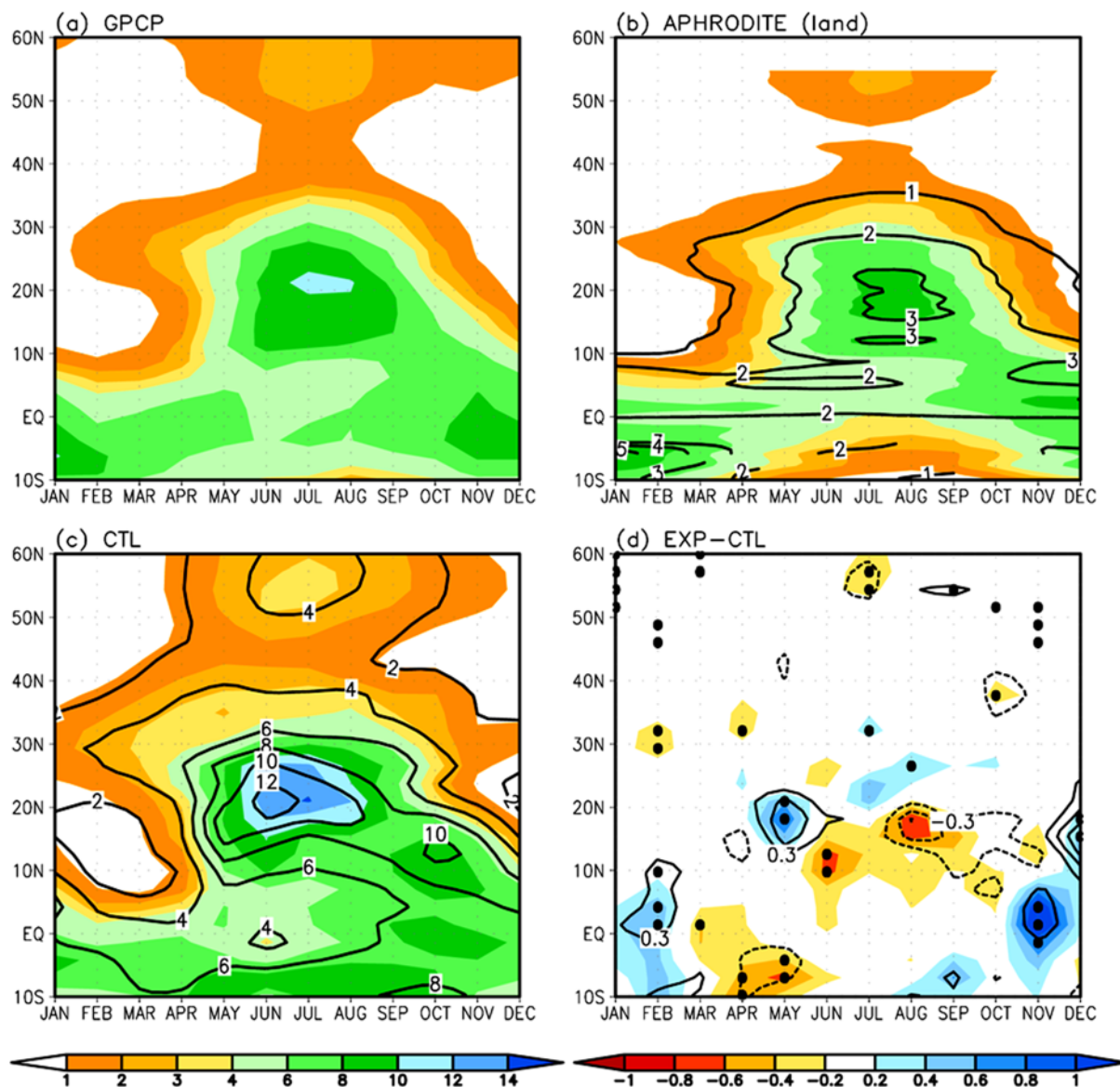


**Fig. 5.** Time-latitude distributions of precipitation (shading) and its daily standard deviation (contours) averaged over the South and Southeast Asian monsoon regions (70–120°E) for: (a) GPCP (1979–2010); (b) APHRODITE (land only, 1951–2003); (c) CTL; and (d) EXP-CTL. Horizontal distributions of the simulated precipitation (contour) and its bias (shading) along with the axis of maximum rainfall (thick red curve) are shown in (e) for the CTL, and (f) for the EXP. Units are  $\text{mm day}^{-1}$  in all plots. The stippled regions in (d) indicate statistically significant changes in rainfall with a 90% confidence level or higher based on a *t*-test.

differences were apparent throughout the South and Southeast Asian monsoon regions. This is also supported by Figs. 2e, f that are presented in the same format as Figs. 2c, d except for the different longitude sector of 90–120°E. The AOD differences of other aerosols (such as BC and sulfate) were trivial, particularly over land, because their surface emissions were prescribed in common between the two numerical simulations. These results suggest that any changes in the aerosol radiative forcings would be induced by the dust and total OC aerosol changes.

Figure 4 shows the differences in aerosol radiative forcing at the surface (ARFS) together with the AOD differences in dust

(thin contour) and total OC (thick contour) particles. Here, the ARFS is defined as the summation of both longwave and shortwave aerosol radiative forcings under clear-sky conditions, although the shortwave component is dominant. During the pre-monsoon season, a reduction of approximately  $0.6\text{--}1.0 \text{ W m}^{-2}$  (and a corresponding surface cooling of approximately  $0.1\text{--}0.3^\circ\text{C}$ , figure not shown) coincided with the higher TAOD for OC, indicating that the dimming effect due to the increased total OC particles was marginally appreciable in the model simulations. Such out-of-phase relationships disappeared with the transition to the rainy season due to a sudden increase in wet deposition.

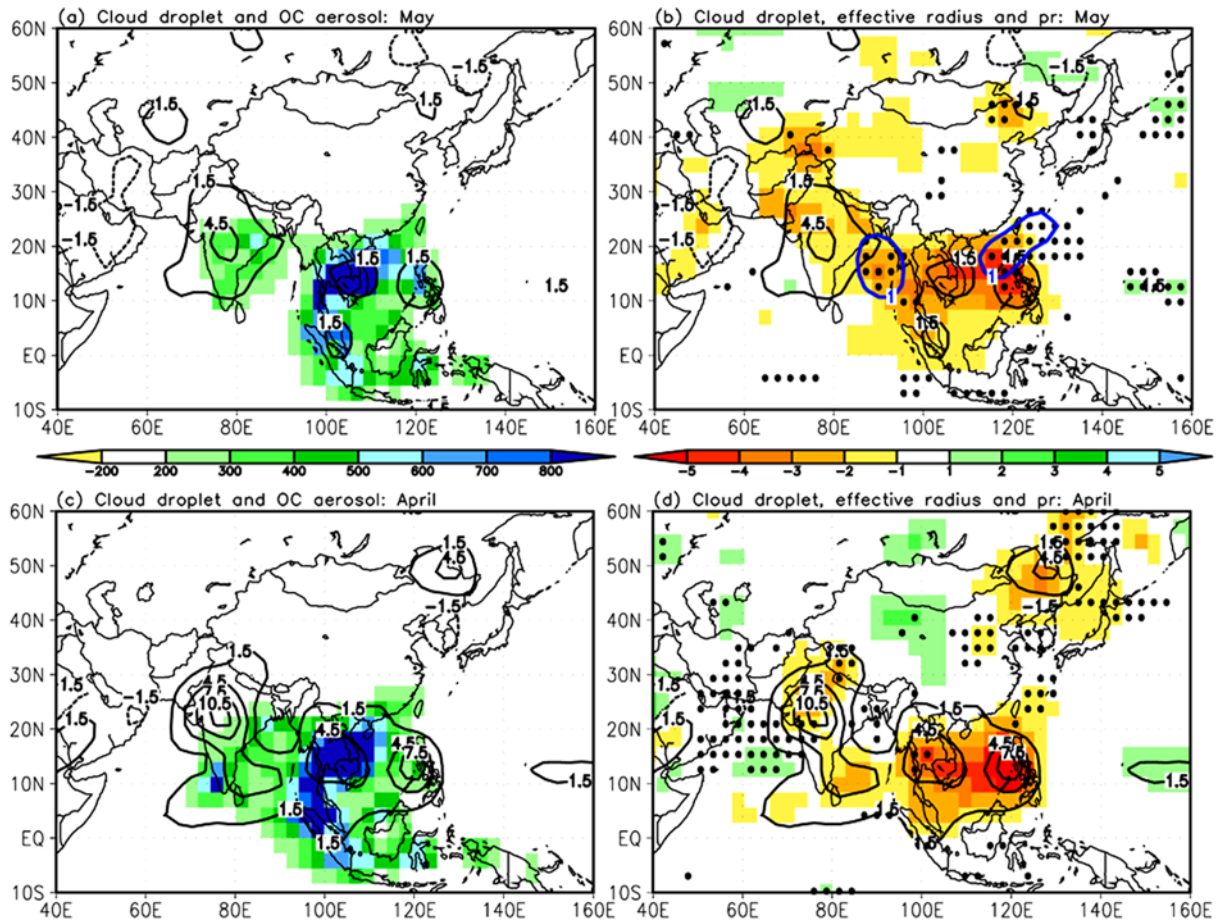


**Fig. 6.** Differences (EXP-CTL) in May in: (a) vertically integrated in-cloud number concentrations of total OC aerosol (shading, #  $\text{cm}^{-3}$ ); and (b) effective radius of cloud water (shading,  $10^{-1} \mu\text{m}$ ) at cloud top level and precipitation (blue contour,  $\pm 1 \text{ mm day}^{-1}$ ). Also shown in both panels is the difference in cloud droplet number concentrations (black contour, #  $\text{cm}^{-3}$ ) at cloud top level. The stippled regions in (b) indicate statistically significant changes in rainfall with a 90% confidence level or higher based on the  $t$ -test. (c)-(d) Same as (a)-(b) except for April. Note that given the same contour interval, no changes were detectable in precipitation during April.

#### 4. Aerosol-cloud interactions

Figures 5a-c present the time-latitude distributions of precipitation (shading) and its daily standard deviation (contour) averaged over the South and Southeast Asian monsoon regions (70-120°E) from observations and the CTL simulation. The observed datasets are monthly Global Precipitation Climatology Project (GPCP) (Huffman *et al.*, 2009) data on a  $2.5^\circ$  grid spacing for 1979-2010 and daily rainfall on a  $0.5^\circ$  resolution in continental Asia for 1951-2003 (Asian Precipitation: Highly-Resolved Observational Data Integration Towards Evaluation of Water Resources, APHRODITE) (Yatagai *et al.*, 2009). The onset of the Asian monsoon varies regionally. Specifically, rainfall starts from early May in southern China (Wang and LinHo, 2002), from mid-May in the IP (Takahashi and Yasunari, 2006), and from early June in India (Wang *et al.*, 2009). Over the area selected for this study, monsoon precipitation usually begins around mid-May, develops during July and August, and declines afterwards (Figs. 5a, b), with a

tendency for enhanced variability (i.e., a large standard deviation) to concur with major rainbands (Fig. 5b). The CTL simulation resembled the observed seasonal march of monsoon precipitation reasonably well. However, the rainfall intensity (variability) was overestimated by approximately 2-4 (4-9)  $\text{mm day}^{-1}$  during the summer season (Fig. 5c). The standard deviation (SD) in simulated daily precipitation was notable over the Arabian Sea to the Indian coast west of the Western Ghats and over the Bay of Bengal to the western coast of Myanmar during the rainy season (data not shown). These spatial patterns of the SD for simulated daily rainfall are similar to the SD for the observations revealed by daily outgoing longwave radiation (Smith and Rutan, 1994). The discrepancy of the SD for simulated daily rainfall is partly derived from the land-only characteristics of APHRODITE. This observational dataset is restricted to a land region, so when it is compared to data for the adjacent ocean, the SD for daily rainfall is relatively small over most of the region except for the limited land area with strong precipitation. As a result,

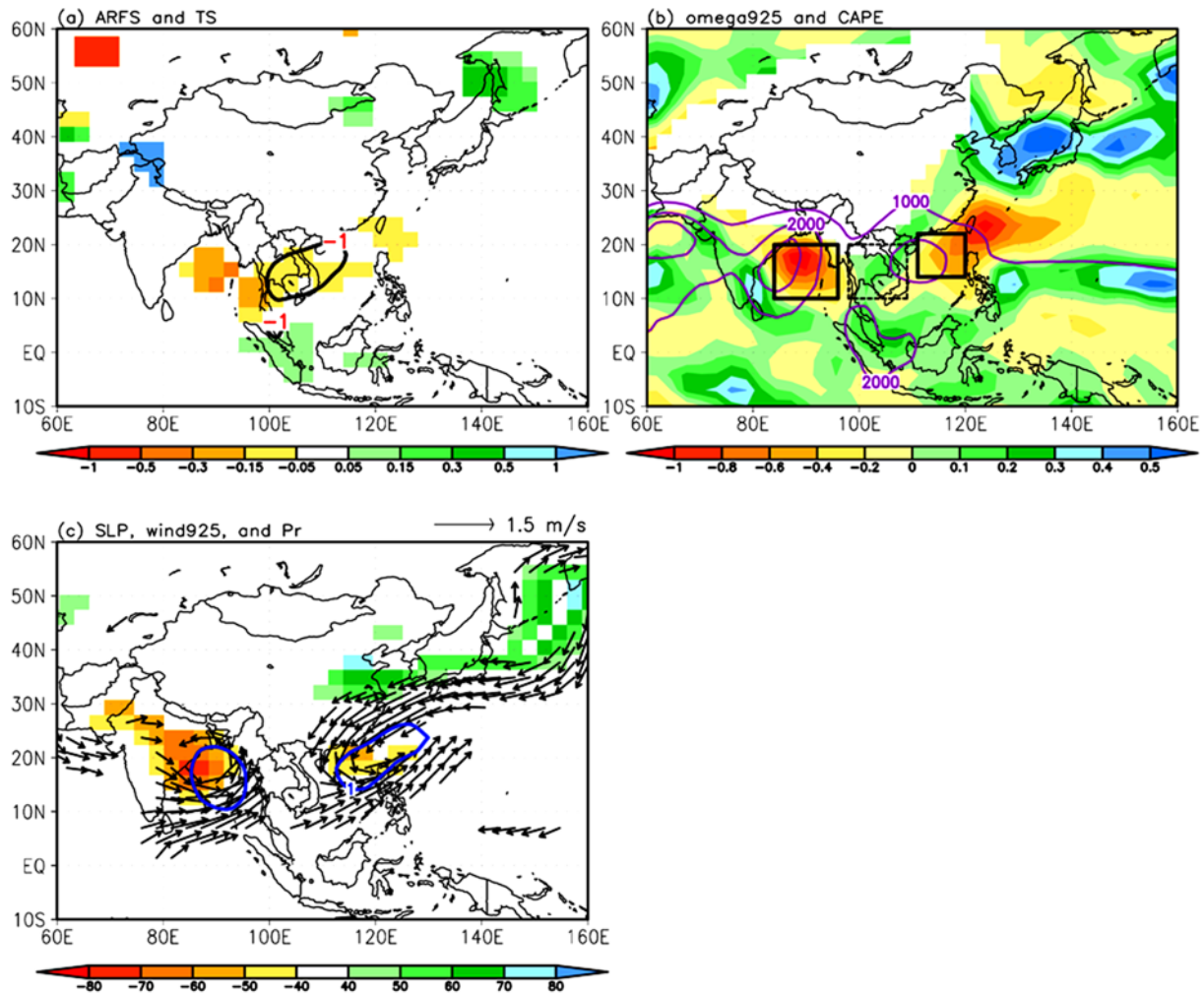


**Fig. 7.** Differences (EXP-CTL) in: (a) aerosol radiative forcing at the surface (contour,  $\text{W m}^{-2}$ ) and surface temperature (shading,  $^{\circ}\text{C}$ ); (b) vertical pressure velocity at 925 hPa (shading,  $10^{-2} \text{ Pa s}^{-1}$ ), and (c) sea-level pressure (shading, Pa), winds at 925 hPa (vectors,  $\text{m s}^{-1}$ ), and precipitation (contour,  $\text{mm day}^{-1}$ ). Also shown in (b) is the climatological convective available potential energy (contour,  $\text{m}^2 \text{ s}^{-2}$ ) derived from the CTL simulation. All plots show calculations for May.

the zonal-mean procedure over only the land region yields a reduction in rainfall variability despite the fact that the SD for daily rainfall from APHRODITE locally amounts to 8–10  $\text{mm day}^{-1}$  at the western coast of India and Myanmar. The overall changes in the simulated summer monsoon precipitation and its daily SD are characterized by an increase in May and a decline in June and August (Fig. 5d). The statistical significance of the rainfall change was tested using a *t*-test. The results indicated that the rainfall changes in May and June are significant at the 90% confidence level or higher. However, it should be noted that the change in SD for daily rainfall is only consistent with the rainfall variation in May. Therefore, we focused mainly on May to investigate cloud-aerosol interactions.

Figure 6a shows the differences in the cloud droplet number concentrations (black contour) and vertically integrated in-cloud number concentrations of total OC aerosol (shading) calculated in May. The total OC aerosol generally increased

over the tropical and subtropical biosphere, and the increase was particularly remarkable in the IP. Accompanied by the changes in total OC, cloud droplet number concentrations increased in the Indian subcontinent, IP, and northern Sumatra, whereas the cloud droplet effective radius was reduced in the regions where total OC aerosol increased (Fig. 6b). These systematic changes were also reproduced in April (Figs. 6c, d), indicating that the parameterization of aerosol-cloud interactions plausibly represents the theoretical process of aerosol nucleation. It should be mentioned that the number concentrations and effective radius of cloud droplets in Fig. 6 were taken from the cloud top level due to the limitation of standard outputs. However, these quantities would be consistent, at least qualitatively, with those obtained by the vertical integration within the cloud. Therefore, the use of cloud-top-level quantities would not compromise the fidelity of the aerosol indirect effect discussed above.

Changes in total OC aerosol obviously play a pivotal role in

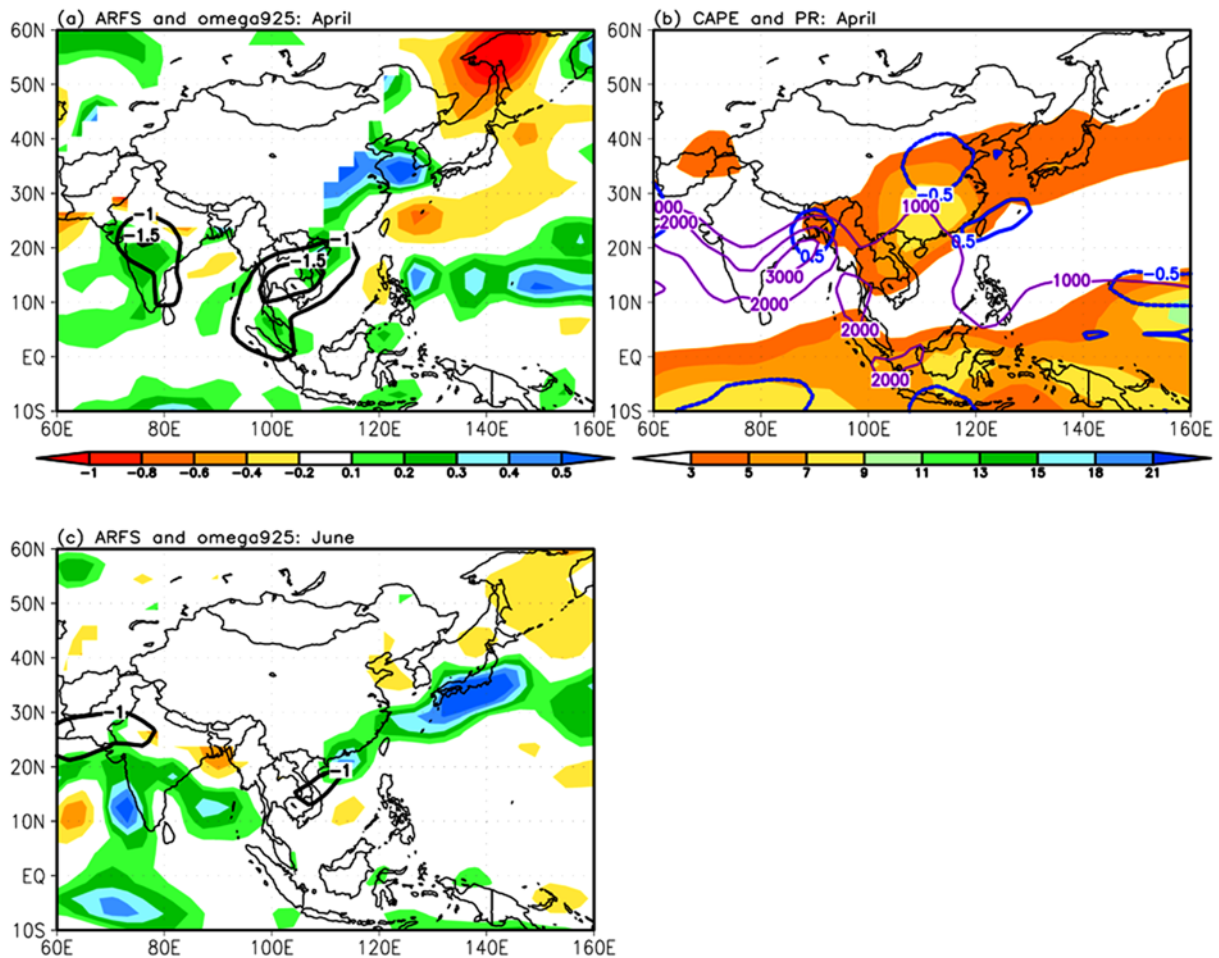


**Fig. 8.** (a) Differences (EXP-CTL) in aerosol radiative forcing at the surface (contour,  $W m^{-2}$ ) and vertical pressure velocity at 925 hPa (shading,  $10^{-2} Pa s^{-1}$ ) in April; (b) April climatology of convective available potential energy (contour,  $m^2 s^{-2}$ ) and precipitation (shading,  $mm day^{-1}$ ) derived from the CTL simulation. Note that the rainfall difference (EXP-CTL) is also shown in (b) using a blue contour with an interval of  $\pm 0.5 mm day^{-1}$ . (c) Same as (a), except data are for June.

the simulated aerosol-cloud interactions that is likely to entail a reduction of precipitation. However, the simulated rainfall increased in and around the regions with a reduced effective radius, particularly in May (Fig. 6b). This finding is at odds with the conceptual model of aerosol-cloud interactions, and deserves further investigation.

### 5. Impact of BVOC-induced aerosols on regional hydrological cycle

The unexpected rainfall changes between the EXP and CTL simulations are prominent in the oceans located on either side of the IP. It should be noted that the IP is a region with a high OC aerosol due to the large BVOC emission (Fig. 6a). This gives rise to a relatively strong ARFS (Fig. 7a). Additionally, variations in the ARFS change with changes in the clear-sky surface incident shortwave radiation in the IP. In other words, the solar radiation reaching the ground declines when the reduction due to the ARFS increases. A correlation coefficient of 0.44 was calculated for this relationship using the May data

for 40 years and a variation of  $\pm 0.3$  in the correlation coefficient met the 95% confidence level based on the *t*-test results. As a consequence, the surface temperature drops slightly in the IP through the aerosol direct effect (Fig. 7a). The surface cooling in the IP induces an anomalous descending motion from the overlying atmosphere, which in turn leads to compensating updrafts in the surrounding oceans (Fig. 7b). The change in vertical motion over the IP is related to changes in surface temperature over the IP with a correlation coefficient of  $-0.3$  (dashed box in Fig. 7b) and a correlation coefficient of  $-0.55$  for the relationship with the change of vertical motion in the adjacent oceans (solid boxes in Fig. 7b). The local maxima of the simulated climatological convective available potential energy (CAPE), controlled primarily by underlying sea surface temperatures (SST) (Graham and Barnett, 1987), tend to reside at either side of the IP and coincide with the regions with anomalous upward motions. Accordingly, although the compensating ascending motion is weak, it results in more active convection that further deepened the surface low, thereby enhancing cyclonic vorticity during the onset of

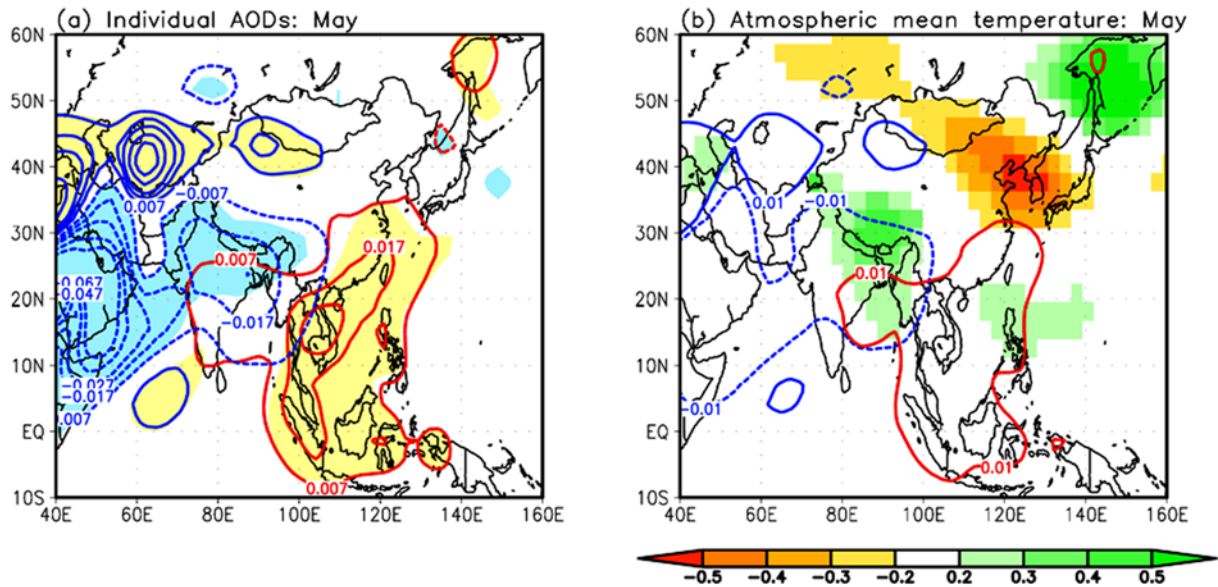


**Fig. 9.** (a) Same as Fig. 2b except data are for May with TAOD differences greater than  $\pm 0.007$  being shaded (positive in yellow and negative in blue); (b) Differences in atmospheric mean (700–200 hPa) temperature in May (shading,  $^{\circ}\text{C}$ ). Contours in (b) denote  $\pm 0.01$  AOD for dust (blue) and OC (red).

the South and South East Asian monsoons (Fig. 7c). This finding suggests that the intensified cyclonic circulations in the surrounding oceans are attributable to the coexistence of abundant CAPE with compensating updrafts. The cooling signals in the Bay of Bengal and South China Sea (Fig. 7a) are indicative of the increased cloudiness associated with the enhanced convection.

The above diagnostic approaches were repeated for April and June. The total OC aerosol from the South Asian tropical rainforest is strongest in April (Figs. 4 and 6c). Changes in the ARFS were therefore most evident in the Indian subcontinent and IP (Fig. 8a). Consequently, the downdraft in the corresponding land areas and rising motion in the nearby regions, especially in the Bay of Bengal where the climatological CAPE has a local maximum, were generally reinforced (Figs. 8a, b). However, the changes in rainfall are either statistically insignificant or negligible (Figs. 5d and 6d), and do not coexist with the major rainbands that appear in southeastern China and south of the Equator (Fig. 8b). It can be speculated that the convective activity, excited by the weak updraft and energized by the CAPE, would result in dry convection unless the frontal activity associated with the monsoon trough sustains convection to form precipitating clouds. The change in ARFS in June was simply too small (Fig. 8c) because of the rapid increase in wet deposition in accordance with more frequent and intense monsoon rainfall. As a result, regional circulation change is not attributable to the change in ARFS in the IP.

## 6. Summary and conclusions

The effects of atmospheric aerosols are among the largest uncertainties in our current understanding of regional and

global environmental change. Therefore, accumulating fundamental scientific insights into the effects of diverse aerosol particles will help promote a quantitative understanding of current conditions and reliable future predictions. This study investigated the climatic response induced by two contrasting estimations of BVOC, one from a pre-existing data base and the other from a more recently developed emission model (MEGAN) (Guenther *et al.*, 2006). Numerical integrations over a 60-year period from 1851 were performed using CGCM. This modeling system enables aerosol particles to affect not only the radiative fluxes but also the formation of cloud droplets.

The use of MEGAN resulted in an overall increase in BVOC emissions from the tropical biosphere located in the South and Southeast Asian regions. Increased BVOC emissions produced a higher SOA oxidation rate, which then led to an enhanced atmospheric loading of OC aerosols. Because BVOC emissions are concentrated over the terrestrial biosphere and the level of atmospheric aerosols is significantly affected by wet deposition, atmospheric OC particles are noticeably enhanced over the Indian subcontinent and IP during the pre- and early-monsoon periods.

As atmospheric aerosols increase, the cloud droplet number concentrations increase, but the size of cloud droplets decreases. All of these changes agree with the conceptual model of the aerosol indirect effect, which in this case should favor the precipitation suppression. However, the model simulations revealed a statistically significant and measurable increase in rainfall in May, which is the onset of monsoon precipitation. Additional analysis suggested that changes in rainfall could deviate from conventional aerosol-cloud interactions on local to regional scales depending upon the following factors: 1) the intensity of aerosol radiative forcing and associated changes in

surface temperature; 2) the extent to which thermally induced vertical motion excites compensating vertical motion in the surrounding regions; and 3) large-scale environmental conditions, such as CAPE and frontal activity associated with monsoon rainbands. The subtle combination of these factors is likely to be able to produce regionally organized rainfall responses that counteract precipitation suppression due to the increased atmospheric aerosol burden.

While the simulated OC radiative forcing demonstrates a typical dimming effect on solar radiation during the onset of the monsoon, absorbing aerosols (such as dust) can heat the atmosphere and draw warm and moist air through an 'elevated heat pump' process (Lau *et al.*, 2006). To investigate whether the competing effect of dust aerosol possibly influences the simulated changes, the individual differences in AOD were calculated once again for May (Fig. 9a) together with the atmospheric mean (700-200 hPa) temperature change (Fig. 9b). The results revealed that the troposphere warms in regions with a reduced AOD due to dust, especially over the TP. Because the elevated heat pump generates tropospheric warming due to an increase in absorbing aerosols, the simulated changes suggest that the dimming effect is dominant or the heat pump mechanism is not realistically reproduced in this particular simulation.

This study attempted to determine a possible pathway for the effects of BVOC-induced aerosol changes on the regional water cycle during the Asian summer monsoon. However, the proposed mechanisms should be considered qualitative and only a working hypothesis. First, the aforementioned processes are only marginally detectable in the model simulations because the BVOC-induced aerosol direct effect, the initiation of the whole processes, was fairly weak. Second, although they are based on physical parameterizations, the chemical processes for atmospheric aerosols and aerosol-induced cloud formation are model-dependent and still need substantial improvement. Third, although the simulation of the Asian summer monsoon is reasonably realistic in our modeling system, it exhibits a non-trivial bias in terms of the intensity and seasonal propagation of monsoon rainbands. These caveats could undermine the robustness of the simulated rainfall response. Additionally, this study did not consider giant CCNs, which play an important role during the evolution of cloud droplet. Giant CCNs, although limited in number, favor the collection process as previously reported in observational studies (e.g., Dusek *et al.*, 2006) as well as in numerical model simulations (e.g., Posselt and Lohmann, 2008). Further studies are therefore necessary with the aid of state-of-the-art climate models incorporating sophisticated representations of aerosol physics, chemistry, and cloud physics.

**Acknowledgments.** We thank the anonymous reviewers for their valuable comments and suggestions. This work was supported by the Environment Research & Technology Development Fund (A0902) from the Ministry of the Environment, Japan. The numerical integrations were carried out on

the Earth Simulator. H.-J. K. also acknowledges support from the APEC Climate Center.

**Edited by:** Song-You Hong, Kim and Yeh

## REFERENCES

- Abdul-Razzak, H., and S. J. Ghan, 2000: A parameterization of aerosol activation: 2. Multiple aerosol type. *J. Geophys. Res.*, **105**, 6837-6844.
- Albrecht, B. A., 1989: Aerosols, cloud microphysics, and fractional cloudiness. *Science*, **245**, 1227-1230.
- Berry, E. X., 1967: Cloud droplet growth by collection. *J. Atmos. Sci.*, **24**, 688-701.
- Bollasina, M. A., Y. Ming, and V. Ramaswamy, 2011: Anthropogenic aerosols and the weakening of the South Asian summer monsoon. *Science*, **334**, 502-505.
- Boucher, O., and U. Lohmann, 1995: The sulfate-CCN-cloud albedo effect: A sensitivity study with two general circulation models. *Tellus*, **47B**, 281-300.
- Charlson, R. J., J. Langner, H. Rodhe, C. B. Leovy, and S. G. Warren, 1991: Perturbation of the northern hemisphere radiative balance by backscattering from anthropogenic sulfate aerosols. *Tellus*, **43AB**, 152-163.
- Chung, S. H., and J. H. Seinfeld, 2002: Global distribution and climate forcing of carbonaceous aerosols. *J. Geophys. Res.-Atmos.*, **107**, 4407, doi:10.1029/2001JD001397.
- Collins, W. J., R. G. Derwent, C. E. Johnson, and D. S. Stevenson, 2002: The oxidation of organic compounds in the troposphere and their global warming potentials. *Climatic Change*, **52**, 453-479.
- Deepak, A., and H. G. Gerber, 1983: Report of the experts meeting on aerosols and their climatic effects, Report of WCP-55, 107 pp., World Meteorological Organization, Geneva, Switzerland.
- Dusek, U., and Coauthors, 2006: Size matters more than chemistry for cloud nucleating ability of aerosol particles. *Science*, **312**, 1375-1378.
- Engelhart, G. J., A. Asa-Awuku, A. Nenes, and S. N. Pandis, 2008: CCN activity and droplet growth kinetics of fresh and aged monoterpene secondary organic aerosol. *Atmos. Chem. Phys.*, **8**, 3937-3949.
- Graedel, T. E., and Coauthors, 1993: A compilation of inventories of emissions to the atmosphere. *Global Biogeochem. Cycles*, **7**, 1-26.
- Graham, N. E., and T. P. Barnett, 1987: Sea surface temperature, surface wind divergence, and convection over tropical oceans. *Science*, **238**, 657-659.
- Guenther, A. B., R. K. Monson, R. Fall, 1991: Isoprene and monoterpene emission rate variability - observations with eucalyptus and emission rate algorithm development. *J. Geophys. Res.-Atmos.*, **96**, 10799-10808.
- Guenther, A., and Coauthors, 1995: A Global-model of natural volatile organic-compound emissions. *J. Geophys. Res.*, **100**, 8873-8892.
- \_\_\_\_\_, T. Karl, P. Harley, C. Wiedinmyer, P. I. Palmer, and C. Geron, 2006: Estimates of global terrestrial isoprene emissions using MEGAN (Model of Emissions of Gases and Aerosols from Nature). *Atmos. Chem. Phys.*, **6**, 3181-3210.
- Hallquist, M., and Coauthors, 2009: The formation, properties and impact of secondary organic aerosol: current and emerging issues. *Atmos. Chem. Phys.*, **9**, 5155-5235.
- Hirabayashi, Y., S. Kanae, I. Struthers, and T. Oki, 2005: A 100-year (1901-2000) global retrospective estimation of the terrestrial water cycle. *J. Geophys. Res.*, **110**, D19101, doi:10.1029/2004JD005492.
- Huffman, G. J., R. F. Adler, D. T. Bolvin, and G. Gu, 2009: Improving the global precipitation record: GPCP Version 2.1. *Geophys. Res. Lett.*, **36**, L17808, doi:10.1029/2009GL040000.
- Jacobson, M., 2001: Strong radiative heating due to the mixing state of black carbon in atmospheric aerosols. *Nature*, **409**, 695-697.

- Johnson, D. B., 1982: The role of giant and ultragiant aerosol particles in warm rain initiation. *J. Atmos. Sci.*, **39**, 448-460.
- Jones, A., D. L. Roberts, and A. Slingo, 1994: A climate model study of indirect radiative forcing by anthropogenic sulfate aerosols. *Nature*, **370**, 450-453.
- Kanakidou, M., and Coauthors, 2005: Organic aerosol and global climate modeling: A review. *Atmos. Chem. Phys.*, **5**, 1053-1123.
- Kuhn, U., and Coauthors, 2004: Seasonal differences in isoprene and light-dependent monoterpene emission by Amazonian tree species. *Global Change Biol.*, **10**, 663-682.
- Lathière, J., C. Hewitt, and D. Beerling, 2010: Sensitivity of isoprene emissions from the terrestrial biosphere to 20th century changes in atmospheric CO<sub>2</sub> concentration, climate, and land use. *Global Biogeochem. Cycle*, **24**, GB1004, doi:10.1029/2009GB003548.
- Lau, K. M., M. K. Kim, and K. M. Kim, 2006: Asian summer monsoon anomalies induced by aerosol direct forcing: The role of the Tibetan Plateau. *Clim. Dynam.*, **26**, 855-864.
- Lean, J., G. Rottman, J. Harder, and G. Kopp, 2005: SORCE contributions to new understanding of global change and solar variability. *Solar Phys.*, **230**, 27-53.
- Meinshausen, M., and Coauthors, 2011: The RCP greenhouse gas concentrations and their extension from 1765 to 2300. *Climatic Change*, **9**, 213-241.
- Menon, S., J. Hansen, L. Nazarenko, and Y. Luo, 2002: Climate effects of black carbon aerosols in China and India. *Science*, **297**, 2250-2253.
- Nakajima, T., M. Tsukamoto, Y. Tsuchima, A. Numaguti, and T. Kimura, 2000: Modeling of the radiative process in an atmospheric general circulation model. *Appl. Opt.*, **39**, 4869-4878.
- Pierce, T. E., and P. S. Waldruff, 1991: Pc-Beis - A personal-computer version of the biogenic emissions inventory system. *J. Air Waste Manage.*, **41**, 937-941.
- Pierce, T., C. Geron, L. Bender, R. Dennis, G. Tonnesen, and A. Guenther, 1998: Influence of increased isoprene emissions on regional ozone modeling. *J. Geophys. Res.*, **103**, 25611-25629.
- Posselt, R., and U. Lohmann, 2008: Influence of giant CCN on warm rain processes in the ECHAM5 GCM. *Atmos. Chem. Phys.*, **8**, 3769-3788.
- Quaas, J., and Coauthors, 2009: Aerosol indirect effects - general circulation model intercomparison and evaluation with satellite data. *Atmos. Chem. Phys.*, **9**, 8697-8717.
- Ramanathan, V., and Coauthors, 2005: Atmospheric brown clouds: Impact on South Asian climate and hydrologic cycle. *Proc. Natl. Acad. Sci.*, **102**, 5326-5333.
- Ramankutty, N., and J. A. Foley, 1999: Estimating historical changes in global land cover: Croplands from 1700 to 1992. *Global Biogeochem. Cycles*, **13**, 997-1027.
- Rosenfeld, D., R. Lahav, A. Khain, and M. Pinsky, 2002: The role of sea spray in cleansing air pollution over ocean via cloud processes. *Science*, **297**, 1667-1670.
- \_\_\_\_\_, J. Dai, X. Yu, Z. Yao, X. Xu, X. Yang, C. Du., 2007: Inverse relations between amounts of air pollution and orographic precipitation. *Science*, **315**, 1396-1398.
- Sanderson, M. G., C. D. Jones, W. J. Collins, C. E. Johnson, and R. G. Derwent, 2003: Effect of climate change on isoprene emissions and surface ozone levels. *Geophys. Res. Lett.*, **30**, 1936, doi:10.1029/2003GL017642.
- Sato, M., J. E. Hansen, M. P. McCormick, and J. B. Pollack, 1993: Stratospheric aerosol optical depth, 1850-1990. *J. Geophys. Res.*, **98**, 22987-22994.
- Smith, G. L., and D. Rutan, 1994: Spatial variability of outgoing longwave radiation. *J. Atmos. Sci.*, **51**, 1808-1822.
- Sudo, K. M., Takahashi, J., Kurokawa, and H. Akimoto, 2002: CHASER: A global chemical model of the troposphere 1. Model description. *J. Geophys. Res.*, **107**, 4339, doi:10.1029/2001JD001113.
- Takahashi, H. G., and T. Yasunari, 2006: A climatological monsoon break in rainfall over Indochina-A singularity in the seasonal march of the Asian summer monsoon. *J. Climate*, **19**, 1545-1556.
- Takemura, T., T. Nakajima, O. Dubovik, B. N. Holben, and S. Kinne, 2002: Single-scattering albedo and radiative forcing of various aerosol species with a global three-dimensional model. *J. Climate*, **15**, 333-352.
- \_\_\_\_\_, T. Nozawa, S. Emori, T. Y. Nakajima, and T. Nakajima, 2005: Simulation of climate response to aerosol direct and indirect effects with aerosol transport-radiation model. *J. Geophys. Res.*, **110**, D02202, doi:10.1029/2004JD005029.
- \_\_\_\_\_, H. Okamoto, Y. Maruyama, A. Numaguti, A. Higurashi, and T. Nakajima, 2000: Global three-dimensional simulation of aerosol optical thickness distribution of various origins. *J. Geophys. Res.*, **105**, 17853-17873.
- \_\_\_\_\_, M. Egashira, K. Matsuzawa, H. Ichijo, R. O'ishi, and A. Abe-Ouchi, 2009: A simulation of the global distribution and radiative forcing of soil dust aerosols at the Last Glacial Maximum. *Atmos. Chem. Phys.*, **9**, 3061-3073.
- Taylor, K. E., R. J. Stouffer, and G. A. Meehl, 2012: An overview of CMIP5 and the experiment design. *Bull. Amer. Meteor. Soc.*, **93**, 485-498.
- Tett, S. F. B., P. A. Stott, M. R. Allen, W. J. Ingram, and J. F. B. Mitchell, 1999: Causes of twentieth-century temperature change near the Earth's surface. *Nature*, **399**, 569-572.
- Textor, C., and Coauthors, 2007: The effect of harmonized emissions on aerosol properties in global models - an AeroCom experiment. *Atmos. Chem. Phys.*, **7**, 4489-4501.
- Tsigaridis, K., and M. Kanakidou, 2007: Secondary organic aerosol importance in the future atmosphere. *Atmos. Environ.*, **41**, 4682-4692.
- Wang, B., and LinHo, 2002: Rainy season of the Asian-Pacific summer monsoon. *J. Climate*, **15**, 386-398.
- \_\_\_\_\_, Q. Ding, and V. Joseph, 2009: Objective definition of the Indian summer monsoon onset using large scale winds. *J. Climate*, **22**, 3303-3316.
- Watanabe, M., and Coauthors, 2010: Improved climate simulation by MIROC5: mean states, variability, and climate sensitivity. *J. Climate*, **23**, 6312-6335.
- Yatagai, A. O. Arakawa, K. Kamiguchi, H. Kawamoto, M. I. Nodzu, and A. Hamada, 2009: A 44-year daily gridded precipitation dataset for Asia based on a dense network of rain gauges. *Sci. Online Lett. Atmos.*, **5**, 137-140, doi:10.2151/sola.2009-035.